Zirconium nitride catalysts surpass platinum for oxygen reduction

Zirconium nitride catalysts surpass platinum for oxygen reduction

Yao Yuan[1,5,6], Jiacheng Wang[3], Samira Adimi[1,5], Hangjia Shen[1,5], Tiju Thomas[4], Ruguang Ma[3], J. Paul Attfield[2,*], Minghui Yang[1,5,*]

[1]Ningbo Institute of Materials Technology and Engineering, Chinese Academy of Sciences, 1219 Zhongguan West Road, Ningbo 315201, P. R. China.

[2] Centre for Science at Extreme Conditions and School of Chemistry, University of Edinburgh, King's Buildings, Mayfield Road, Edinburgh, EH9 3JZ, UK

[3]State key Laboratory of High Performance Ceramics and Superfine Microstructure, Shanghai Institute of Ceramics, Chinese Academy of Sciences, 1295 Dingxi Road, Shanghai 200050, P. R. China.

[4]Department of Metallurgical and Materials Engineering, Indian Institute of Technology Madras Adyar, Chennai 600036, Tamil Nadu, India.

[5]Center of Materials Science and Optoelectronics Engineering, University of Chinese Academy of Sciences, Beijing 100049, P. R. China.

[6]University of Chinese Academy of Sciences, 19A Yuquan Rd, Shijingshan District, Beijing 100049, P. R. China.

Yao Yuan and Jiacheng Wang contributed equally to this work.

Corresponding Authors

*E-mails: j.p.attfield@ed.ac.uk and myang@nimte.ac.cn

Platinum (Pt) based materials are important components of microelectronic sensors, anticancer drugs, automotive catalytic converters and electrochemical energy conversion devices.[1] Pt is currently the most common catalyst used for the oxygen reduction reaction (ORR) in devices such as fuel cells and metal-air batteries,[2,3] although scalable use is restricted by the scarcity, cost, and vulnerability to poisoning of Pt.[4-6] Here we show that nanoparticulate zirconium nitride (ZrN) can replace and even surpass Pt as a catalyst for ORR in alkaline environments. As-synthesised ZrN nanoparticles exhibit a high oxygen reduction performance with the same activity as that of a widely-used Pt on carbon commercial catalyst. Both materials show the same half-wave potential ($E_{1/2}$ = 0.80 V) and ZrN has higher stability ($\triangle E_{1/2}$ = -3 mV) than the Pt/C ($\triangle E_{1/2}$ = -39 mV) after 1000 ORR cycles in 0.1 M KOH. ZrN is also shown to deliver greater power density and cyclability than Pt/C in a zinc-air battery. Replacement of Pt by ZrN is likely to reduce costs and promote usage of electrochemical energy devices, and ZrN may also be useful in other catalytic systems.

Most electrochemical energy conversion devices use catalysts to deliver power at acceptable rates.[7] Power delivery from fuel cells and metal-air batteries is largely limited by the relatively sluggish oxygen reduction reaction (ORR)[8,9] in which molecular oxygen is electrochemically reduced with concomitant generation of an electrical potential. ORR is one of the most fundamental reactions involved in energy conversion devices since oxygen is a sustainable and accessible oxidant,[10] and has faster kinetics under alkaline conditions.[11] Alkaline polymer electrolyte membrane fuel cells are of current interest due to potential advantages of a less corrosive environment, more diverse fuels, decreased fuel crossover rates, improved water

management and better mitigation of CO poisoning compared to acidic devices.[12] Currently the most widely used and efficient ORR catalyst is platinum (Pt), usually on a carbon support.[2] Pt is scarce (37 ppb in Earth's crust) [13] and expensive (US$ 28.3 g^{-1} as the 2018 average price),[14] so much effort has been devoted to using Pt more efficiently or finding alternative platinum-free catalysts.[3,5,15] However, low-cost materials that offer high catalytic activity and durability have remained elusive, so industrial use is still largely limited to Pt-based catalysts for fuel cells, e.g. in automotive applications.[16] Other carbon-supported materials including metal-N/C and metal-free catalysts do not meet requirements for practical use in energy devices due mainly to instability issues. [5,17,18] Unsupported transition metal nitrides have been considered as promising substitutes due to their high (metallic) electrical conductivity, good corrosion resistance, and thermal and electrochemical stabilities.[19,20] However, previously reported materials (see Supplementary Table 1) have not proved competitive with Pt.[21-23] Results presented here show that a ZrN catalyst based on cheap earth-abundant elements (2018 price for Zr metal is ~US$ 38.8 kg^{-1})[24] is a highly-attractive alternative to Pt for ORR in alkaline environments, offering a combination of low cost, high activity, and superior stability.

ZrN is conventionally synthesized by heating ZrO_2 in ammonia at temperatures above 1200 ºC,[25] which promotes aggregation and grain growth resulting in low catalytic activity. In this work we have produced fine ZrN nanoparticles (NPs) using a urea-glass route at moderate temperatures (see Methods, Fig. 1 and Extended Data Fig. 1). A pure crystalline phase of ZrN with the cubic rocksalt structure was obtained. The NPs (45 ± 16 nm in diameter; 28 m^2 g^{-1} surface area) exhibit near-spherical morphology with few intergrowths and have large-scale chemical homogeneity (Fig.

1c, Extended Data Figs. 2 and 3). Zr 3d X-ray photoelectron spectroscopy (XPS) shows that exposure to air results in the formation of a thin (<1 nm) oxynitride or oxide surface layer (Fig. 1b and Extended Data Fig. 4), but no distinct surface phases are seen by high-resolution transmission electron microscopy (HR-TEM) or energy dispersive X-ray spectroscopy (EDX) mapping (Fig. 1d-h). The thin oxidized layer protects the ZrN particles from further oxidation and does not offer any discernible hindrance to fast electron transport.[26]

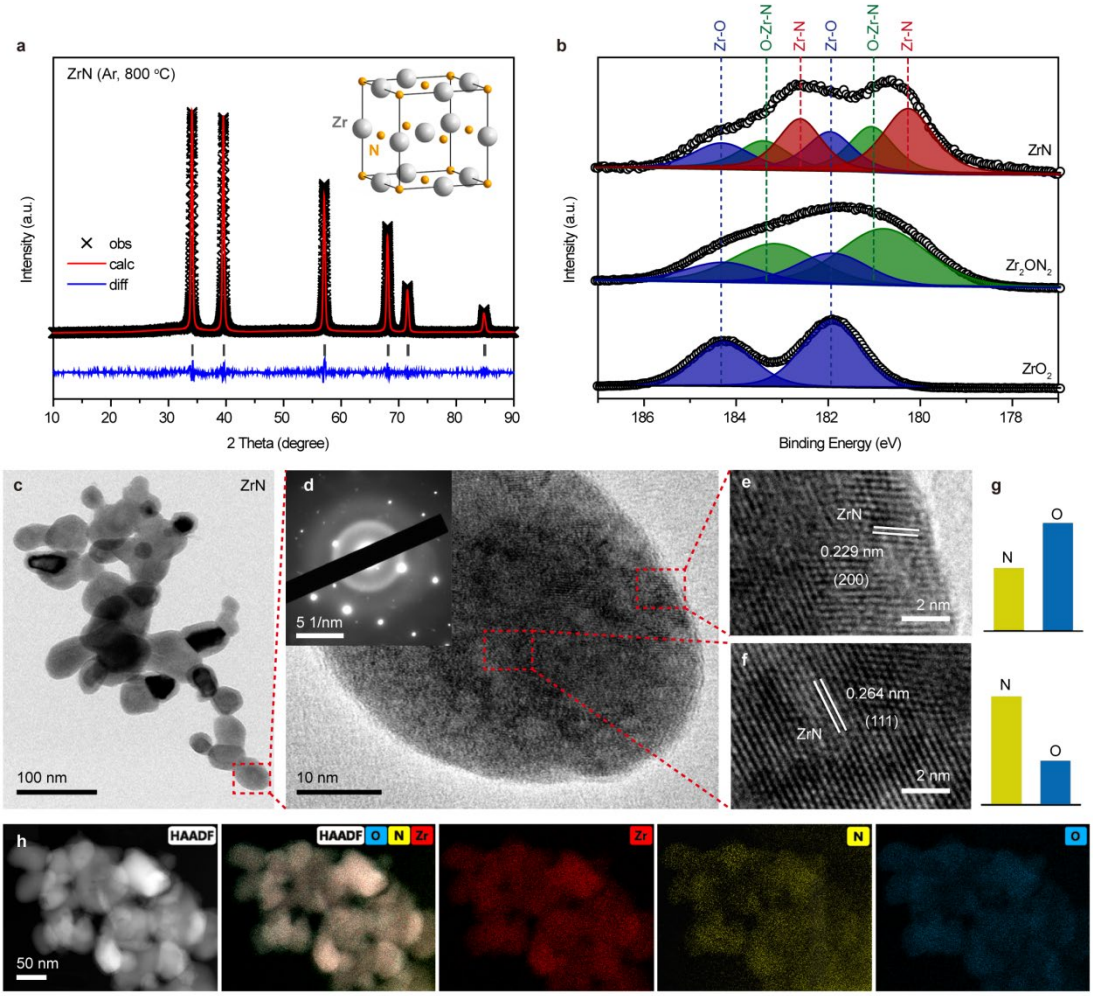

Fig. 1 | Characterisation of ZrN nanoparticles. a, The Rietveld fitted XRD pattern of ZrN NPs. **b,** XPS spectra of ZrN, Zr_2ON_2 and ZrO_2 in the Zr 3d region, showing the presence of surface ZrO_2 and Zr_2ON_2 on the ZrN NPs. **c** and **d,** TEM images with the corresponding selected area electron diffraction (SAED) pattern inset in **d**. **e** and **f,** HR-TEM images of selected regions of the particle shown in **d**. Lattice fringes are visible with d-spacings of 0.229 and 0.264 nm corresponding to the (200) and (111)

planes of cubic ZrN. **g,** Relative N and O contents measured by EDX in the latter two regions, showing a higher oxygen content in region **e** at the oxidized NP surface. **h,** High-angle annular dark field-scanning TEM (HAADF-STEM) and EDX mapping images of Zr, N and O showing a homogenous elemental distribution.

Electrochemical experiments demonstrate that ZrN NPs have a comparable ORR performance to commercial Pt/C. Cyclic voltammetry (CV) measurements (Fig. 2a, Extended Data Fig. 5) show that the cathodic peak for reduction of oxygen by ZrN occurs at the same potential of 0.79 V, relative to the reversible hydrogen electrode (RHE) potential, as for commercial Pt/C. A rotating disk electrode (RDE) was used to assess ORR catalytic activity through linear sweep voltammetry (LSV) which measures the kinetics of the interfacial redox reaction without limitations of diffusion. The LSV curves for the two materials (Fig. 2b) are very similar, with onset potentials of 0.89 V for ZrN and 0.93 V for Pt/C, and they both have the same half-wave potential ($E_{1/2}$ = 0.80 V). It is notable that ZrN has more positive onset and half-wave potentials than those of previously reported metal nitrides,[20-23] with values that are well-matched to those of Pt. The measured ZrN potentials are found to be reproducible to ±10 mV (Extended Data Fig. 5). The turnover frequencies at 0.8 V of our ZrN catalyst and the commercial Pt/C were calculated to be 0.188 and 0.056 s^{-1} respectively, see Supplementary Methods 1, demonstrating that ZrN has a large number of active surface sites for ORR.

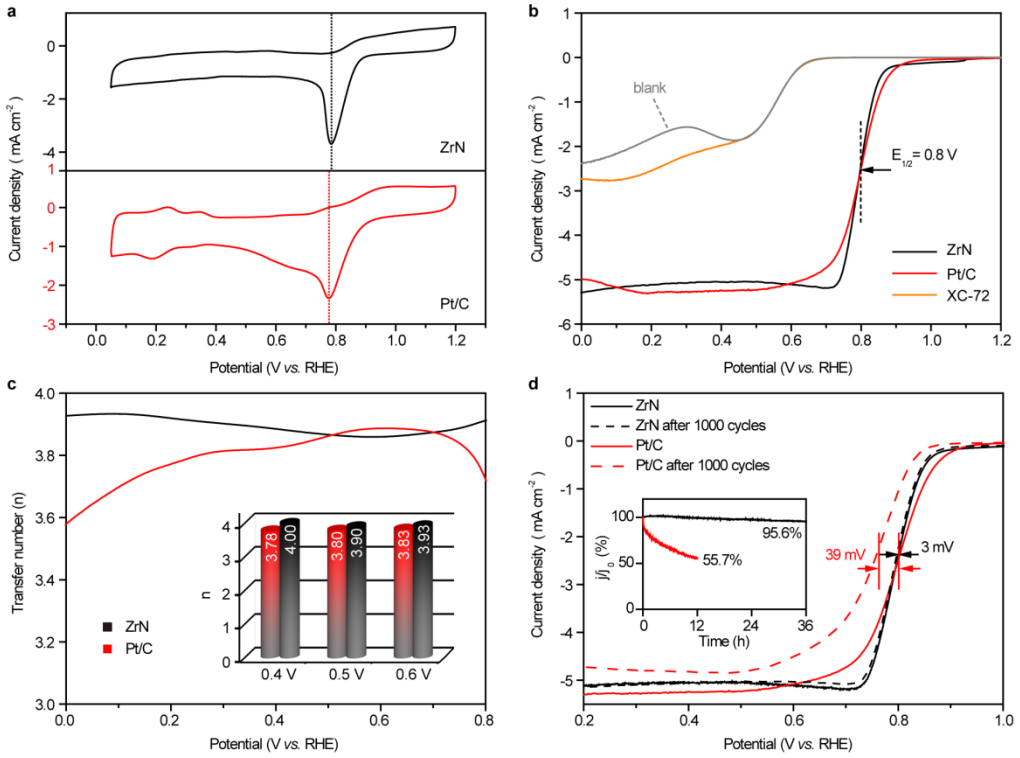

Fig. 2 | ORR catalysis properties of nanoparticulate ZrN and Pt/C in O_2-saturated 0.1 M KOH solution. a, CV curves at a scan rate of 50 mV s^{-1}. **b,** LSV curves of the catalyst samples, the XC-72 carbon support, and a blank glassy carbon disk electrode (GCDE, electrode rotating speed: 1600 rpm; scan rate: 10 mV s^{-1}). **c,** Electron transfer numbers calculated from the rotating ring-disk electrode measurements, and from Koutechy-Levich plots at fixed potentials in the inset bar chart. **d,** Polarization curves before (solid curves) and after (dashed curves) accelerated degradation tests, with chronoamperometric responses at a constant potential (inset).

The number of electrons *n* transferred to each O_2 molecule during ORR is important as full n = 4 reduction to OH^- without formation of H_2O_2 as the product of two-electron reduction is desirable. Koutechy-Levich (K-L) plots obtained from LSV measurements at differing speeds of rotation (Extended Data Fig. 6) are linear, indicating first-order reaction kinetics with respect to the concentration of dissolved oxygen.[8] Values of n = 3.9 - 4.0 for the ZrN NPs at potentials of 0.4 – 0.6 V are very close to the ideal for four-electron reduction, and are slightly greater than

corresponding values of $n \approx 3.8$ for Pt/C (inset of Fig. 2c). Additional rotating ring-disk electrode measurements also reveal very high selectivity of ZrN for the four-electron pathway. The calculated H_2O_2 yield is found to be below ~10 % at potentials from 0 to 0.8 V with calculated transfer numbers $n = 3.9$ - 4.0 for ZrN throughout this range (Fig. 2c). In contrast, the transfer number for Pt/C drops significantly at potentials below 0.3 or above 0.7 V. Hence ZrN outperforms Pt/C as a four-electron ORR catalyst across this range of potentials (Extended Data Fig. 7). A gold disk electrode (GDE) was also used as the working electrode to exclude the possibility that carbon is responsible for the catalytic activity. The GDE results agree with those obtained using a glassy carbon disk electrode (GCDE), as shown in Extended Data Fig. 8, demonstrating that the activity of the ZrN catalyst is intrinsic.

The durability of an electrocatalyst is a crucial parameter that determines application in a real system. Pt-based catalysts gradually degrade owing to dissolution, aggregation and surface oxidation, especially in alkaline conditions.[3,27] The long-term durability of our ZrN catalyst for ORR was assessed by a standard accelerated degradation test (ADT) which was carried out by cycling the potential between 0.6 and 1.2 V in a 0.1 M KOH solution exposed to air at room temperature. The half-wave potential $E_{1/2}$ after 1000 cycles for ZrN exhibits a small shift of about -3 mV, compared to a -39 mV shift for the commercial Pt/C (Fig. 2d). Even after 8000 cycles, the shift in $E_{1/2}$ is only -7 mV for ZrN (Extended Data Fig. 7e). This demonstrates an excellent durability for the ZrN NPs, exceeding that of commercial Pt/C in an alkaline medium. The chronoamperometric responses of ZrN NPs and Pt/C were also compared at 0.5 V with a RDE rotating at 1600 rpm (inset of Fig. 2d). The ZrN electrode shows a 4% decrease in current after 36 h, whereas the Pt/C catalyst

displays a much greater current loss of 44% after only 12 h. The stability of the ZrN NPs was further evaluated by chronoamperometry in strongly alkaline conditions, showing a current drop of only 12% after 18 h in 6 M KOH solution (Extended Data Fig. 7f). The excellent stability of our catalyst in comparison to Pt/C makes nanoparticulate ZrN a very promising practical material for ORR and other important catalytic reactions in alkaline conditions.

To assess performance in a real electrochemical device, ZrN has been tested in comparison to Pt/C as the cathode in a zinc-air battery,[5] fabricated as shown in Extended Data Fig. 9. The two batteries have similar voltage-current curves (Fig. 3a) and the highest power density for the ZrN-based battery of 132 mW cm^{-2} exceeds that of 122 mW cm^{-2} for the Pt/C-driven battery. Both batteries were also operated at a current density of 10 mA cm^{-2} for 100 h to check the stability of the air cathode, and the ZrN battery displayed a much smaller voltage decrease (21 mV) than the Pt/C battery (46 mV) as shown in Fig. 3b. These results directly demonstrate the applicability of ZrN NP electrodes in zinc-air batteries, and similar advantages over Pt/C are expected in alkaline fuel cells. ZrN may also be useful for electrochemical reactions under acidic conditions, where Zr-based catalysts have sometimes been found to be active.[28]

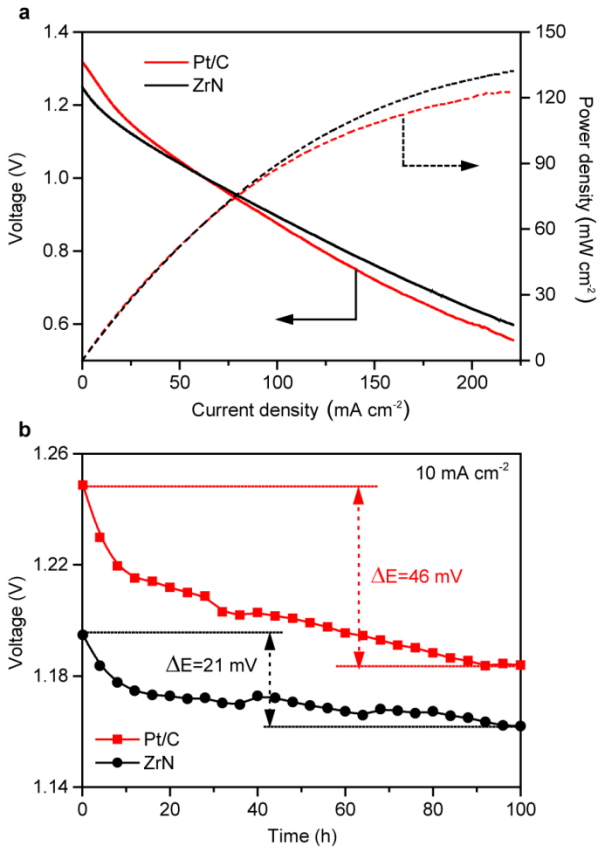

Fig. 3 | Zinc-air batteries using nanoparticulate ZrN or Pt/C cathodes. a, Discharge polarization curves and the corresponding power densities. **b,** Discharge curves at a constant current density of 10 mA cm^{-2}.

Previous studies of Pt alloys with 3d metals show that the d-states play a crucial role in determining the catalytic properties.[29] The calculated band structures of ZrN and Pt both have strong d-orbital contributions to the states at the Fermi level (Extended Data Fig. 10), although it is not apparent from the bulk electronic structure why ZrN outperforms other transition metal nitrides with similar band structures as an ORR catalyst.[22] Surface electronic structure and the interactions between Zr sites and oxide species through active sites for O_2 adsorption are likely to be key ingredients,[29,30] and so surface electronic structure has been explored as shown in Supplementary Methods 2 and Supplementary Table 2. Our calculations show that the Zr-terminated (111) surface of ZrN is the most stable low-index surface and has a very similar oxygen

adsorption energy to the Pt-(111) surface, which is a key factor that accounts for the high ORR activity. The calculated clean and O-adsorbed (111) surface structures of ZrN and the corresponding Electron Localization Function (ELF) plots are shown in Fig. 4. The ELF shows high electron localization at a small Zr-O cluster around the surface oxide, while highly delocalized states are available at the nitride from the sub-surface layer. These may provide the active sites for catalysis.

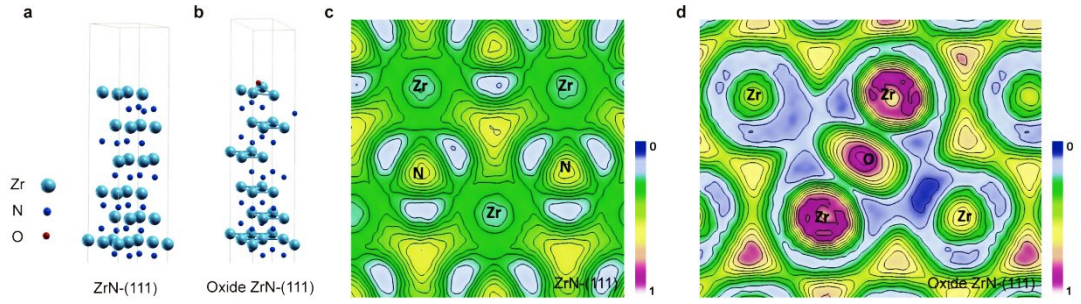

Fig. 4 | ZrN-(111) surface structures and Electron Localization Functions showing effects of adsorbed oxide. a and b, The crystal structures of clean and oxide-adsorbed ZrN-(111) surfaces and underlying layers. The large light blue and small dark blue balls show Zr and N atoms respectively, while the O atom is shown by a small red ball on surface **b**. **c and d**, The Electron Localization Functions (ELF) of the clean and oxide-adsorbed surfaces. **d** shows high electron localization at the surface oxide, adjacent to delocalized states at the nitride from the sub-surface layer, which may provide the active sites for catalysis.

To conclude, we have shown that nanoparticulate ZrN is an attractive replacement for Pt-catalysts for the oxygen reduction reaction under alkaline conditions in electrochemical devices. ZrN NPs exhibit outstanding activity, excellent long-term stability, and promote almost ideal four-electron reduction of oxygen. None of the hitherto reported nitrides or other catalysts shows this combination of performance and durability. Extensive use of ZrN in metal-air batteries, fuel cells and related electrochemical energy conversion and storage devices is anticipated. This work will also stimulate further investigations of inexpensive metal nitride catalysts that not just match but outperform Pt-group metals.

References

1 Chen, A. & Holt-Hindle, P. Platinum-based nanostructured materials: synthesis, properties, and applications. *Chem. Rev.* **110**, 3767-3804 (2010).

2 Shao, M., Chang, Q., Dodelet, J. P. & Chenitz, R. Recent Advances in Electrocatalysts for Oxygen Reduction Reaction. *Chem. Rev.* **116**, 3594-3657 (2016).

3 Li, M. *et al.* Ultrafine jagged platinum nanowires enable ultrahigh mass activity for the oxygen reduction reaction. *Science* **354**, 1414-1419 (2016).

4 Cao, B. *et al.* Cobalt molybdenum oxynitrides: synthesis, structural characterization, and catalytic activity for the oxygen reduction reaction. *Angew. Chem. Int. Ed.* **52**, 10753-10757 (2013).

5 Chung, H. T. *et al.* Direct atomic-level insight into the active sites of a high-performance PGM-free ORR catalyst. *Science* **357**, 479-484 (2017).

6 Wei, W. *et al.* Nitrogen-doped carbon nanosheets with size-defined mesopores as highly efficient metal-free catalyst for the oxygen reduction reaction. *Angew. Chem. Int. Ed.* **53**, 1570-1574 (2014).

7 Chu, S., Cui, Y. & Liu, N. The path towards sustainable energy. *Nat. Mater.* **16**, 16-22 (2016).

8 Liang, Y. *et al.* Co_3O_4 nanocrystals on graphene as a synergistic catalyst for oxygen reduction reaction. *Nat. Mater.* **10**, 780-786 (2011).

9 Bashyam, R. & Zelenay, P. A class of non-precious metal composite catalysts for fuel cells. *Nature* **443**, 63-66 (2006).

10 Kumar, A., Ciucci, F., Morozovska, A. N., Kalinin, S. V. & Jesse, S. Measuring oxygen reduction/evolution reactions on the nanoscale. *Nat. Chem.* **3**, 707-713 (2011).

11 Shen, H. *et al.* Oxygen Reduction Reactions of Fe-N-C Catalysts: Current Status and the Way Forward. *Electrochem. Energ. Rev.* https://doi.org/10.1007/s41918-019-00030-w (2019).

12 Zhou, T. *et al.* A review of radiationgrafted polymer electrolyte membranes for alkaline polymer electrolyte membrane fuel cells. *J. Power Sources* **293**, 946–975 (2015).

13 Nørskov, J. K. *et al.* Origin of the overpotential for oxygen reduction at a fuel-cell cathode. *The Journal of Physical Chemistry B* **108**, 17886-17892 (2004).

14 http://www.lme.com

15 Snyder, J., Fujita, T., Chen, M. W. & Erlebacher, J. Oxygen reduction in nanoporous metal-ionic liquid composite electrocatalysts. *Nat. Mater.* **9**, 904-907 (2010).

16 Hiroyuki, Y., Mikio, K. & Hisao, A. Toyota Fuel Cell System (TFCS). *World Electric Vehicle Journal* **7**, 85-92 (2015).

17 Zhao, Y. *et al.* Few-layer graphdiyne doped with sp-hybridized nitrogen atoms at acetylenic sites for oxygen reduction electrocatalysis. *Nat. Chem.* **10**, 934-931 (2018).

18 D, G. *et al.* Active sites of nitrogen-doped carbon materials for oxygen reduction reaction clarified using model catalysts. *Science* **16**, 361-365 (2016).

19 Giner, J. & Swette, L. Oxygen Reduction on Titanium Nitride in Alkaline Electrolyte. *Nature* **211**, 1291-1292 (1966).

20 Pan, Z. *et al.* Hollow and porous titanium nitride nanotubes as high-performance catalyst supports for oxygen reduction reaction. *J. Mater. Chem. A* **2**, 13966-13975 (2014).

21 Cao, M., Di, Z., Cui, Z., Wang, S. & Qin, J. VN hollow spheres assembled from porous

nanosheets for high-performance lithium storage and oxygen reduction reaction. *J. Mater. Chem. A* **4**, 7914-7923 (2016).

22 Youn, D. H. *et al.* A highly efficient transition metal nitride-based electrocatalyst for oxygen reduction reaction: TiN on a CNT–graphene hybrid support. *J. Mater. Chem. A* **1**, 8007-8015 (2013).

23 Dong, Y. & Li, J. Tungsten nitride nanocrystals on nitrogen-doped carbon black as efficient electrocatalysts for oxygen reduction reactions. *Chem. Commun.* **51**, 572-575 (2014).

24 https://www.smm.cn/metal/minor-metals

25 Bo, F. & Lian, G. Synthesis of Nanocrystalline Zirconium Nitride Powders by Reduction–Nitridation of Zirconium Oxide. *J. Am. Ceram. Soc.* **87**, 696-698 (2010).

26 Miloiev, I., Strehblow, H. H., GaberLEek, M. & Naviniek, B. Electrochemical Oxidation of ZrN Hard (PVD) Coatings Studied by XPS *Surf. Interface. Anal.* **24**, 448-458 (1996).

27 Huang, X. *et al.* High-performance transition metal-doped Pt_3Ni octahedra for oxygen reduction reaction. *Science* **348**, 1230-1234 (2015).

28 Doi, S., Ishihara, A., Mitsushima, S., Kamiya, N. & Ota, K. Zirconium-Based Compounds for Cathode of Polymer Electrolyte Fuel Cell. *J. Electrochem. Soc*. **154**, B362-B369 (2007).

29 Stamenkovic, V. *et al.* Changing the Activity of Electrocatalysts for Oxygen Reduction by Tuning the Surface Electronic Structure. *Angew. Chem. Int. Ed.* **45**, 2897-2901 (2006).

30 Vojvodic, A. & Norskov, J. K. New design paradigm for heterogeneous catalysts. *Natl. Sci. Rev.* **2**, 140-149 (2015).

Acknowledgements

This work is supported by Natural Science Foundation of China (Grant No. 21471147), National Key Research and Development Plan (Grant No. 2016YFB0101205), and Key Program of the Chinese Academy of Sciences (Grant No. KFZD-SW-320). JW thanks the Equipment Research Program (6140721050215) for financial support. MY would like to thank the National "Thousand Youth Talents" program of China and Ningbo 3315 program for support. JPA thanks EPSRC for support.

Author contributions

YY and JW contributed equally to this work. MY and JPA conceived and coordinated the research. YY synthesized and characterized the materials; SA performed electronic structure calculations; and YY, JW, HS, TT, and RM carried out and analyzed the electrochemical measurements and co-wrote the paper with MY and JPA. All authors discussed the results and commented on the manuscript.

Methods

Synthesis of ZrN. All of the chemical reagents are analytical grade without further purification. Zirconium nitride (ZrN) nanoparticles were prepared by a urea-glass route using zirconium chloride ($ZrCl_4$) as the metal source. In a typical synthesis, 1 g of $ZrCl_4$ (≥99%, Aladdin Industrial Corporation) powder was dispersed in ethanol (2 mL) to reach the targeted concentration to form a stable and clear solution. Urea (1 g, ≥99%, Aladdin Industrial Corporation) was added and the mixture was stirred until the urea was dissolved and the solution was completely clear. The solution was aged for 12 h in order to complete the complexation of Zr by urea and the resulting colorless transparent sols were heated at 10 °C min^{-1} under an argon flow (100 mL min^{-1}) in a tubular furnace up to 800 ºC, held at that temperature for 3 h, furnace cooled to room temperature, and passivated by being held for 2 h under the same argon flow. The slow initial heating is important to avoid excessive foaming and eruptive release of solvent from the glassy precursor. The reductive urea decomposes into NH_2, NH_3, HNCO, and H_2NCO groups at elevated temperatures >200 ºC leading to formation of ZrN.[31,32] The urea also acts as a stabilizing agent to control the nanoparticle size.[33] No purifications before or after the nitridation treatment are needed and no byproducts or side reactions are observed. This method has the advantages of simplicity, low cost and nontoxicity of reagents, and high catalytic activity of the as-prepared product,[33,34] and so is very promising for scaling up to larger applications.

Syntheses of Zr_2ON_2 and ZrO_2. Pure polycrystalline samples were synthesized using the same precursor and heating cycle as above, but heating

and cooling under an ammonia flow (100 mL min^{-1}) to obtain Zr_2ON_2, or in air for ZrO_2. After cooling, Zr_2ON_2 was passivated under flowing Ar (20 mL min^{-1}) for 2 h.

Pt/C. A commercial sample of Pt on XC-72 carbon support (20 wt% Pt, HiSPEC 3000, Johnson Matthey) was used throughout.

Materials characterization.

Fourier Transform Infrared (FT-IR) spectra of KBr powder-pressed pellets were recorded with a Thermo NICOLET 6700 spectrometer. Spectra used to explore the synthesis mechanism are shown in Extended Data Fig. 1. Urea molecules are coordinated to zirconium while chloride anions are in the outer coordination sphere. Coordination of urea though oxygen is determined particularly by the decrease of a carbonyl stretching frequency at 1684 cm^{-1}, and by the decrease in wavenumber of the $\nu(CO)+\delta(NH_2)$ vibration.[35]

X-ray powder diffraction (XRD) measurements were performed using a powder X-ray diffractometer (Rigaku Miniflex 600) with Cu-K_α radiation (λ = 1.54178 Å) in a 2θ range from 10° to 90° scanning at 1° min^{-1}. The XRD patterns of ZrN samples match well with the reported cubic ZrN phase (space group: Fm-3m (No. 225), a = 4.58 Å) (Fig. 1a). The average ZrN particle size is estimated to be 46 nm from the Scherrer broadening of diffraction peaks, in good agreement with the SEM result below. Corresponding zirconium oxide and oxynitride XRDs are presented in Extended Data Fig. 2.

The morphologies and microstructures of the samples were characterized by scanning electron microscopy (SEM) (JSM-7800F, Japan) and transmission electron microscopy (TEM) (FEI Tecnai F20) measurement. Particles of ZrN exhibit a near-spherical morphology in SEM images (Extended Data Fig. 2). The diameters of 200 randomly selected particles in the SEM image of Extended Data Fig. 2c were measured as shown in the histogram in Extended Data Fig. 2d. The mean particle diameter is 45 nm with a standard deviation in the distribution of 16 nm. Similar morphology is observed in the TEM (Fig. 1c) and the selected area electron diffraction (SAED) pattern has discrete spots, further demonstrating the crystalline character of the ZrN NPs (Fig. 1d). High-resolution TEM (HRTEM), high-angle annular dark field-scanning TEM (HAADF-STEM) and energy dispersive X-ray (EDX) elemental mapping images were further used to characterize the samples, as shown in Fig. 1. The surface area of 27.7 m^2 g^{-1} for ZrN was measured by the Brunauer-Emmett-Teller (BET) method as shown in Extended Data Fig. 3. Nitrogen adsorption and desorption isotherms were measured at -196 °C using a Quadrasorb SI system.

X-ray photoelectron spectroscopy (XPS, VG ESCALAB MKII) with Mg K_α as the excitation source was used to analyze surface valence of the materials with carbon as an internal standard (C 1s=284.8 eV). XPS analyses indicated that the samples contain Zr, O, and N without other impurity elements as shown in Fig. 1b and Extended Data Fig. 4. For the ZrO_2 NPs, the Zr 3d spectrum shows two peaks at 184.3 and 182.0 eV, which can be assigned to the binding energies of the $3d_{5/2}$ and $3d_{3/2}$ orbitals of Zr^{4+}. For Zr_2ON_2, the Zr 3d XPS peaks can be

deconvoluted into four peaks, the peaks at 184.5 and 182.1 eV are characteristic peaks of surface ZrO_2, while the peaks at 183.1 and 180.8 eV are assigned to Zr_2ON_2. The high-resolution Zr 3d XPS peaks of the ZrN NPs indicate that three Zr species are present, with surface ZrO_2 and Zr_2ON_2 observed, and peaks at 180.2 eV($3d_{5/2}$) and 182.6 eV($3d_{3/2}$) evidencing the underlying ZrN. N and O 1s XPS spectra are shown in Extended Data Fig. 4.

Raman spectra were obtained on a confocal microprobe Raman system (Renishaw inVia Reflex). As shown in Extended Data Fig. 4i, the spectrum of ZrN exhibits two strong peaks at 150-260 and 497 cm^{-1}, due to acoustic and optical phonons respectively. Weaker peaks around 653 and 980 cm^{-1} are consistent with second-order scattering.[36,37] None of the characteristic peaks from carbon are observed in the 1300-1600 cm^{-1} region showing that the ZrN sample does not contain significant amounts of carbon.

Electrochemical tests. The ORR electrochemical measurements were carried out in a three-electrode system using a rotating disk electrode (RDE) (PINE Instrument) with an electrochemical workstation (CHI660E, CH Instrument). A glassy carbon disk electrode (GCDE) or a gold disk electrode (GDE) with a diameter of 5 mm was used as the support for the working electrode. The GCDE was polished with α–Al_2O_3 powder of decreasing sizes (1.0 μm to 50 nm), and then ultrasonically washed with deionized water and absolute ethanol. Typically, 5 mg catalyst mixed with 30 μL Nafion solution were dispersed in 1 mL of isopropanol solution and sonicated for 1 h to form a homogeneous ink. 5 μL of the dispersion was dropped onto the GCDE/GDE surface using a micropipette and dried at ambient temperature. The reference

electrode was Ag|AgCl/KCl (saturated) electrode and the counter electrode was a Pt wire. All the potentials were calibrated to the reversible hydrogen electrode (RHE) potential calculated from the equation: E(RHE) = E(Ag/AgCl) + (0.197 + 0.059 pH)V, and all potentials in this Letter are quoted *vs.* RHE.

The CV curves of samples were measured in an Ar or O_2-saturated 0.1 M KOH solution using the same RDE but without rotation. Polarization curves were recorded using linear sweep voltammetry (LSV) with a scan rate of 10 mV s^{-1} in 0.1 M KOH solutions after purging with O_2 for at least 30 min. The H_2O_2 yield and electron transfer number *n* were calculated from the equations Yield(H_2O_2) = $2(I_R/N)/[(I_R/N) + I_D]$ and $n = 4I_D/[(I_R/N) + I_D]$, where I_D and I_R are the disk and ring currents, and the ring collection efficiency was $N = 0.37$. For an accelerated durability test (ADT), the electrodes were cycled between 0.6 and 1.2 V in O_2 saturated KOH (0.1 M) with a scan rate of 100 mV·s^{-1}. A graphite counter electrode was used in the ADT instead of Pt wire to avoid redepositing Pt on the working electrode. CV and ORR polarization curves were collected simultaneously during some cycles to monitor the degradation of the electrocatalyst. For chronoamperometric tests, a static overpotential was fixed during continuous ORR process to obtain the curve of time dependence of the current density.

The Zn-air battery tests were performed at an operating temperature of 25 °C, in which 6 M KOH with 0.2 M $Zn(CH_3COO)_2$ was employed as electrolyte and a polished Zn foil was used as the anode electrode. The air cathode was made by drop-casting the catalyst (ZrN or Pt/C) ink onto hydrophilic carbon paper (HESEN HCP120) with a loading of 1.0 mg cm^{-2}. The catalyst ink was prepared by mixing

catalysts with a solution of 5 wt% Nafion (Dupont) and isopropanol. The gas diffusion layer on the other side of the carbon paper allows O_2 from ambient air to reach the catalyst. The polarization curves were obtained using a CHI660E electrochemical workstation, and the galvanostatic discharge measurements were performed on a NEWARE battery testing system.

Computational methodology. Electronic structure calculations were performed using Density Functional Theory (DFT) as implemented in the Quantum Espresso Package[38] while the generalized gradient approximation–projector augmented wave (GGA-PAW) pseudopotentials are adopted for our Plane-Wave calculations. The convergence threshold for a self-consistent energy was 10^{-6} a.u. per unit cell, while the residual forces on each atom are less than 10^{-4} eV and the optimized cutoff energy is 40 Ry. Tetrahedral integration and the projection of calculated wave functions over orthogonalized atomic pseudo-orbitals were used to calculate the Density of States (DOS) and the Partial Density of States (PDOS). Details of surface calculations are shown in Supplementary Methods.

Data availability

The data supporting the findings of this study are available from the corresponding authors upon request.

References

31 Qiu, Y. & Gao, L. Metal-Urea Complex-A Precursor to Metal Nitrides. *J. Am. Ceram. Soc.* **87**, 352-357 (2010).

32 Giordano, C., Erpen, C., Yao, W. & Antonietti, M. Synthesis of Mo and W carbide and nitride nanoparticles via a simple "urea glass" route. *Nano Lett.* **8**, 4659-4663 (2008).

33 Giordano, C., Erpen, C., Yao, W., Milke, B. & Antonietti, M. Metal Nitride and Metal Carbide Nanoparticles by a Soft Urea Pathway. *Chem. Mater.* **21**, 5136-5144 (2009).

34 Penland, R. B., Mizushima, S., Curran, C. & Quagliano, J. V. Infrared Absorption Spectra of Inorganic Coördination Complexes. X. Studies of Some Metal-Urea Complexes. *J. Am. Chem. Soc.* **79**, 1575-1578 (1957).

35 Molinari, V., Giordano, C., Antonietti, M. & Esposito, D. Titanium Nitride-nickel Nanocomposite as Heterogeneous Catalyst for the Hydrogenolysis of Arylethers. *J. Am. Chem. Soc.* **136**, 1758-1761 (2014).

36 Chen, X. J. *et al.* Pressure-induced phonon frequency shifts in transition-metal nitrides. *Phys. Rev. B* **70**, 2199-2208 (2004).

37 Spengler, W. & Kaiser, R. First and second order Raman scattering in transition metal compounds. *Solid State Commun.* **18**, 881-884 (1976).

38 Wentzcovitch, P. G. *et al.* QUANTUM ESPRESSO: a modular and open-source software project for quantum simulations of materials. *J. Phys. Condens. Matter.* **21**, 395502 (2009).